FULL PAPER

The Impacts of Cation Stoichiometry and Substrate Surface Quality on Nucleation, Structure, Defect Formation, and Intermixing in Complex Oxide Heteroepitaxy–LaCrO₃ on SrTiO₃(001)

L. Qiao, K. H. L. Zhang, M. E. Bowden, T. Varga, V. Shutthanandan, R. Colby, Y. Du, B. Kabius, P. V. Sushko, M. D. Biegalski, and S. A. Chambers*

The ability to design and fabricate electronic devices with reproducible properties using complex oxides is critically dependent on our ability to controllably synthesize these materials in thin-film form. Structure-property relationships are intimately tied to film and interface composition. Here the effect of cation stoichiometry on structural quality and defect formation in LaCrO₃ heteroepitaxial films prepared using molecular beam epitaxy is reported. From first principles the regions of stability of various candidate defects, along with the predicted effects of these defects on structural parameters, are calculated as a function of Cr and O chemical potential. Epitaxial LaCrO₃ films readily nucleate and remain coherently strained on SrTiO₃(001) over a wide range of La-to-Cr atom ratios, but La-rich films are of considerably lower structural quality than stoichiometric and Cr-rich films. Cation imbalances are accompanied by anti-site defect formation. Cation mixing occurs at the interface for all La-to-Cr ratios investigated and is not quenched by deposition on SrTiO₃(001) at ambient temperature. Indiffused La atoms occupy Sr sites. Intermixing is effectively quenched by using molecular beam epitaxy to deposit LaCrO₃ at ambient temperature on defect free Si(001). However, analogous pulsed laser deposition on Si is accompanied by cation mixing.

1. Introduction

Since the discovery of high-temperature superconductivity in cuprates at the end of the last century, complex oxide films and multilayers have been of significant interest in condensed-matter physics and materials science, as well as electronic device technology, because of their wide range of physical properties. The interactions of multiple intrinsic order parameters (charge, spin, orbital, and lattice), combined with extrinsic properties (e.g., reduced dimensionality and thermal and photon activation) have produced a rather complex phase space of properties. In this space, a broad range of functionalities can be present including superconductivity, photoconductivity, photovoltaic effects, ferromagnetism, ferroelectricity and multiferroic behavior. The rich range of optical, dielectric, electronic and magnetic behavior in these materials, along with their structural, chemical and thermal stabilities, endow these materials with potential new functionalities not possible in conventional semiconductors.

Reproducible and reliable oxide electronic devices cannot be fabricated and the mechanisms for their operation cannot be understood unless control over epitaxial film growth and heterojunction formation is achieved. Historically, the development of robust and controllable epitaxial film growth methods has led to the maturation of other electronic materials technologies. For example, the perfecting of III-V semiconductor heteroepitaxy by molecular beam epitaxy (MBE) and metal organic chemical vapor deposition in the 1980s and 1990s has led to the invention and development of a number of novel device technologies based on these materials. Complex oxides are now viewed as one of the next frontiers in electronic materials. Pulsed laser deposition (PLD) is a very popular deposition method for complex oxide films because of its relatively low cost and ease of use. MBE has been less commonly used for complex oxides because it is

Dr. L. Qiao, K. H. L. Zhang, Dr. S. A. Chambers
Fundamental and Computational Sciences Directorate
Pacific Northwest National Laboratory
Richland, WA, 99354, USA
E-mail: sa.chambers@pnnl.gov
Dr. L. Qiao, Dr. M. D. Biegalski
Center for Nanophase Materials Sciences
Oak Ridge National Laboratory
Oak Ridge, TN, 37831, USA

Dr. M. E. Bowden, Dr. T. Varga, Dr. V. Shutthanandan,
Dr. R. Colby, Dr. Y. Du, Dr. B. Kabius
Environmental Molecular Sciences Laboratory
Pacific Northwest National Laboratory
Richland, WA, 99354, USA
Prof. P. V. Sushko
Department of Physics and Astronomy and London Centre
for Nanotechnology
University College London
Gower Street, London, WC1E 6BT, UK

**ADVANCED
FUNCTIONAL
MATERIALS**

www.afm-journal.de

FULL PAPER

*Materials
Views*

www.MaterialsViews.com

generally more expensive and more difficult to use. A significant number of publications claiming exotic and novel electronic phenomena have appeared based mostly on PLD-grown material. However, the rigor in film growth and materials characterization associated with the development of III-V based materials has in general not been present in much of the complex oxide activity. A good example is the discovery of conductivity at the interface of polar and nonpolar insulating perovskites, such as LaAlO₃/SrTiO₃ (LAO/STO).[1–4] Explanations of this unexpected behavior range from classic electronic reconstruction,[5–7] based on the assumptions of fully stoichiometric films and atomically perfect interfaces, to oxygen vacancy formation[8–10] and unintentional doping by cation intermixing.[11–14] However, despite several years of work along with hundreds of publications and conference presentations, consensus is still lacking, quite possibly as a result of significant sample variation from lab to lab due to a lack of control over film and heterojunction growth, and inadequate materials characterization.

The question of stoichiometry in complex oxide films and its relationship to functional properties is largely unexplored. In PLD growth, it is often tacitly assumed that composition is preserved in going from the ablation target to the film. However, this assumption may not be valid, particularly when the substrate is exposed to only one part of the plume.[15–17] Evidence for changes in the cation atom ratios during laser ablation has recently been generated for perovskites such as SrTiO₃ (STO),[18,19] BaTiO₃,[20] PbTiO₃, LaAlO₃,[21,22] SrRuO₃,[23] LaMnO₃,[24] and SrMnO₃.[25] Moreover, slight deviations in composition have proven to induce dramatic changes in the structure and properties of some complex oxides.[26,27] Composition control in PLD is generally thought to be achievable by tuning the laser energy density to exceed the threshold ablation energy for the various cations in the target.[28,29] However, due to the complexity of the interaction between incoming laser photons and the target, our knowledge about the physics of the ablation process is limited.

In comparison, composition control is more straightforward in MBE, at least in principle. Because each metal source is independently controlled, one can tune film composition by tuning metal evaporation rates and accounting for the dependences of sticking coefficients at the growth temperature. Moreover, MBE has the potential to produce films of higher purity and lower defect density than PLD owing to the higher purity of commercially available metals compared to oxides, and the lower characteristic energies of atomic species emanating from effusion cells compared to those associated with ablation targets. The downside of oxide MBE is its higher cost and greater level of difficulty. Films are often grown under oxygen-rich conditions using a source of activated O₂.[30] As a result, precise composition control remains a major challenge, especially when the different cations exhibit large differences in oxygen affinity. Extents of surface oxidation of the hot metal charges in effusion cells vary considerably across the periodic chart, and can have a profound effect on evaporation and sublimation rates. In situ flux monitoring techniques such as quartz crystal microbalance (QCO) and atomic absorption technology,[31,32] as well as indirect methods such as reflection high-energy electron diffraction (RHEED),[33,34] have been used to monitor fluxes and film stoichiometry for some complex oxides. However, the sensitivity

and reproducibility for each of these monitoring techniques are material dependent. None of these have enough sensitivity for all elements typically found in complex oxides to allow composition control down to the atomic percent level, at least thus far.

Here we report on the effect of composition variation for LaCrO₃ (LCO) heteroepitaxy on STO(001) by MBE, examining film nucleation, structure, morphology, interfacial mixing and defect generation. We have previously demonstrated that stoichiometric LCO grows coherently on STO(001) up to a thickness of at least 900 Å and that polar LCO/nonpolar STO interfaces are insulating.[35,36] The relatively small in-plane lattice mismatch (≈0.5% for pseudocubic LCO) facilitates the heteroepitaxy of LCO on STO(001), and allows the effect of film composition on structure to be systematically investigated. We demonstrate that crystalline quality, film surface morphology and defect density are sensitive to the La-to-Cr cation ratio. We also discuss the role of substrate surface quality and deposition method in promoting interfacial mixing.
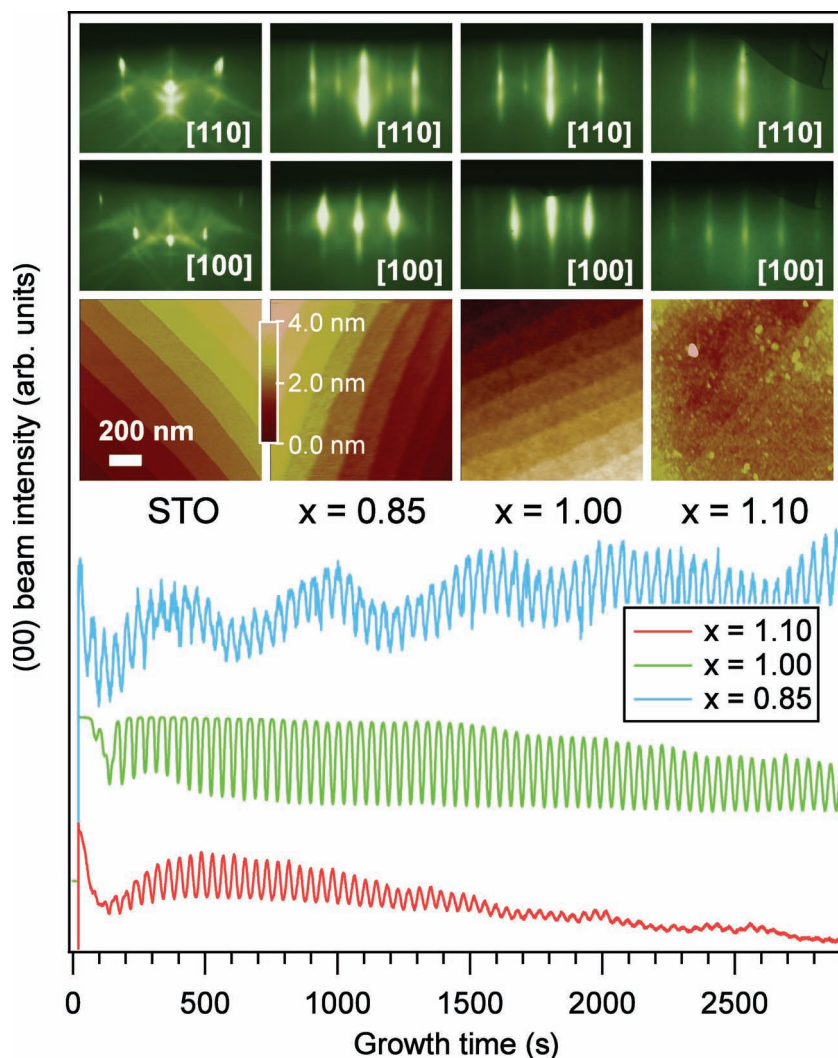
2. Results and Discussion

2.1. Film Growth and In Situ Characterization

A set of RHEED specular beam intensity oscillations as a function of growth time are shown in **Figure 1** for 500 Å-thick Cr-rich (La:Cr = x = 0.85), stoichiometric (x = 1.00) and La-rich (x = 1.10) LCO films. For the stoichiometric film, the RHEED oscillations persist with uniform amplitude throughout the entire film growth, indicating a stable and persistent 2D layer-by-layer growth. Persistent RHEED oscillations were also observed for the Cr-rich film, although a low-frequency modulation is superimposed on the oscillations. In contrast, the oscillation amplitude decays to near zero for the La-rich film, indicating the cessation of 2D layer-by-layer growth.

We also show in Figure 1 RHEED patterns along both [110] and [100] crystallographic directions and atomic force microscopy (AFM) images for an HF-etched and tube furnace annealed STO(001) substrate, and 500 Å films with different compositions. The surfaces of both the stoichiometric and Cr-rich films retain the step-terrace structure of the substrate with a minimum step height of ≈4 Å, consistent with the persistent RHEED oscillations. In contrast, the La-rich film surface roughens considerably, obliterating the terrace-step structure of the substrate, consistent with the decay of the RHEED intensity oscillations. The RHEED patterns for both stoichiometric and Cr-rich films are strong and streaky, indicative of well-ordered and flat surfaces. Additionally, both exhibit a (2 × 2) surface reconstruction. However, the surface of La-rich film exhibits a much weaker (1 × 1) pattern, revealing considerably more disorder associated with the rough surface seen in AFM.

X-ray photoelectron spectroscopy (XPS) core-level and valence band (VB) spectra are shown in **Figure 2** for a series of films with x ranging from 0.92 to 1.25. A low-energy electron flood gun had to be used to compensate the positive surface charge accompanying photoemission when the film surfaces were found to be insulating. In order to directly compare binding energies, the O 1s peaks (not shown) were all shifted to 530.0 eV.

Materials
Views
www.MaterialsViews.com

ADVANCED
FUNCTIONAL
MATERIALS
www.afm-journal.de

FULL PAPER

Figure 1. RHEED specular beam intensity oscillations as a function of growth time for 500 Å La-rich (La:Cr = x = 1.10), stoichiometric (x = 1), and Cr-rich (x = 0.85) LCO films. Also shown are RHEED patterns along both [110] and [100] directions and AFM images for these films and a clean STO(001) substrate.

For each specimen, the same shift was then applied to La 4d, Cr 2p and VB spectra. The La 4d and Cr 2p binding energies and line shapes are characteristic of La^{3+} and Cr^{3+} for all cation ratios, and change little with x. The VB spectra for x ranging from 0.92 to 1.11 changes in ways that are largely predictable based on the known electronic structure of LCO. The feature at $\approx$2 eV, dominated by Cr 3d t$_{2g}$ with an admixture of O 2p character,[35,36] drops in intensity relative to the rest of the VB with increasing x as the Cr fraction in the film drops. However, the overall shape of the VB remains characteristic of that for LCO for x = 0.92 to 1.11, and there is no evidence for secondary phases in these data. In contrast, the portion of the VB from $\approx$3 to $\approx$9 eV undergoes a substantial change in shape for x = 1.25. The valley fills in and the shoulder at $\approx$8 eV is no longer resolved. Even though the RHEED patterns (not shown) remain characteristic of those of LCO, this portion of the VB becomes very similar in appearance to that of La$_2$O$_3$, which is also shown in Figure 2, right-hand panel. The

latter spectrum was measured from an La$_2$O$_3$ reference film, prepared by depositing La metal in excess O$_2$ on Si(001) at ambient temperature. From these data, we conclude at x = 1.25, at least some of the excess La is excluded from the lattice and forms a disordered secondary phase of La$_2$O$_3$.

2.2. Film Crystallography and Defect Formation

X-ray diffraction (XRD) data reveal that representative films with x values ranging from 0.85 to 1.10 contain epitaxial LCO as the majority phase, and do not reveal the presence of any detectable secondary phases (see Supporting Information Figure 1). We show in **Figure 3**a a representative {110} ϕ scan for a stoichiometric LCO film and the STO substrate. The presence of four-fold symmetry, together with overlapping film and substrate Bragg peaks, reveal the expected cube-on-cube structure with the epitaxial relationship $(001)_{LCO}\|(001)_{STO}$ and $[110]_{LCO}\|[110]_{STO}$. The ϕ scans for the other films are the same.

Figure 3b shows a set of θ–2θ scans near the (002) Bragg peak for four approximately stoichiometric films with different film thicknesses: 100 Å (x = 1.00), 200 Å (x = 0.97), 500 Å (x = 1.00) and 900 Å (x = 0.94). All four films exhibit finite thickness fringes with periods that scale with film thickness. The Bragg peak for the 100 Å film peak is rather weak and very broad because of the small thickness, but the thickness fringes are nevertheless clearly resolved. Thickness fringes are seen in films with uniform thickness and out-of-plane lattice constant. Thus, the presence of these fringes in all films reveals good crystallinity. We also performed (002) rocking-curve measurements for 200, 500 and 900 Å films (see Supporting Information Figure 2). All films exhibit the same rocking-curve shape and full-width at half-maximum (FWHM) value as their respective STO substrates, thus indicating that film quality is limited by substrate quality. Typical FWHM values range from 0.008° to 0.08°. Both out-of-plane and in-plane lattice parameters were calculated by simultaneously fitting the (00l) (l = 1, 2, 3), (113), (123) and (114) peaks (see Supporting Information Figure 3). The resulting lattice parameters for all four films plus those for a stoichiometric 15 u.c. LCO/STO (as determined by RBS channeling) are plotted in Figure 3c. All films are coherently strained to the substrate, and the c lattice parameter depends on cation ratio, as seen in the inset.

In Figure 3d we compare the structural quality and out-of-plane lattice parameters of stoichiometric and nonstoichiometric films. The Cr-rich film exhibits oscillations slightly weaker than those of the stoichiometric film, indicating slightly reduced crystal quality. In contrast, the La-rich film shows

**ADVANCED
FUNCTIONAL
MATERIALS**
www.afm-journal.de

Materials
Views
www.MaterialsViews.com
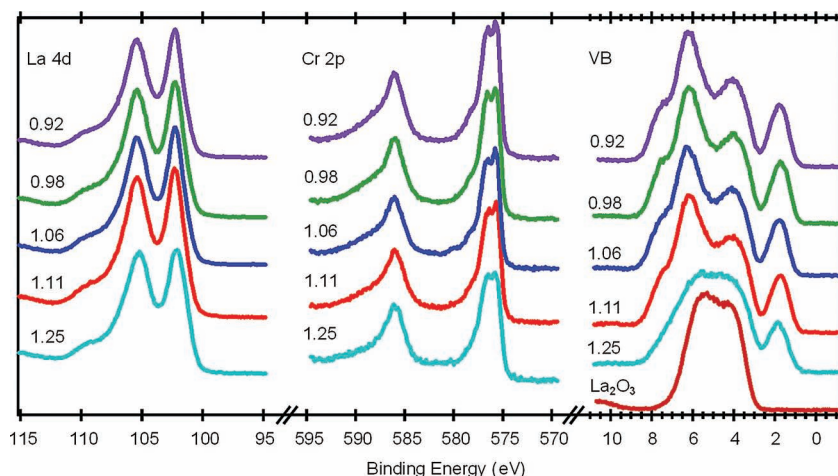
Figure 2. Core-level and valence band XPS data measured at normal emission for a series of LCO(001) films with x ranging from 0.92 to 1.25.

almost no oscillation amplitude, revealing poorer ordering and/ or a rougher surface. Rocking-curve measurements (see Supporting Information Figure 2) confirm that the Cr-rich and stoichiometric films are of comparable quality since their (002) rocking-curve widths are the same as those of their substrates, whereas the La-rich film exhibits a larger width than its substrate. As seen in the inset to Figure 3c, the three films portrayed in Figure 3d have the same a value as STO, revealing a critical thickness in excess of 500 Å, independent of stoichiometry from $x = 0.85$ to 1.10. Point defects associated with non-stoichiometry may provide strain relief in lieu of line defects, thereby enabling a larger critical thickness than nominally expected for 0.5% in-plane lattice mismatch.

We also see from Figure 3d that the Bragg angle for these films decreases with increasing x, revealing a concomitant increase in the out-of-plane lattice parameter, c (Figure 3c). In order to gain some understanding of this trend, we carried out first-principles calculations to determine the effect of various kinds of defects on the value of c for LCO that is coherently strained to the substrate. We focus on Cr and La defects: i) anti-site defects in which a La atom occupies a Cr site (La_{Cr}) and a Cr atom occupies a La site (Cr_{La}), ii) neutral La and Cr vacancies, and iii) neutral La and Cr interstitials. The anti-site defects do not require charge compensation since Cr and La have the same oxidation state, while the vacancies and interstitials produce three holes and three extra electrons, respectively. Here we considered one defect per $2\sqrt{2}a \times 2\sqrt{2}a \times 4c$ supercell, which corresponds to $x = 0.94$ for Cr_{La}, $x = 0.97$ for Cr vacancy and La interstitial, $x = 1.03$ for La vacancy and Cr interstitial, and $x = 1.06$ for La_{Cr}. Substitutional Cr in Cr_{La} displaces from the La site and gives rise to the axial and equatorial configurations, as expected for strained epitaxial LCO. Hence, the formation energies of Cr_{La} and the values of c were averaged with the corresponding Boltzmann factors for $T = 300$ K. An interstitial Cr atom is located in the BO_2 planes that are either parallel or perpendicular to the plane of the interface. In our case, the difference of the total energies calculated for these configurations is significant enough that only the former can be considered. Similarly, only the site in the AO plane parallel to the plane of

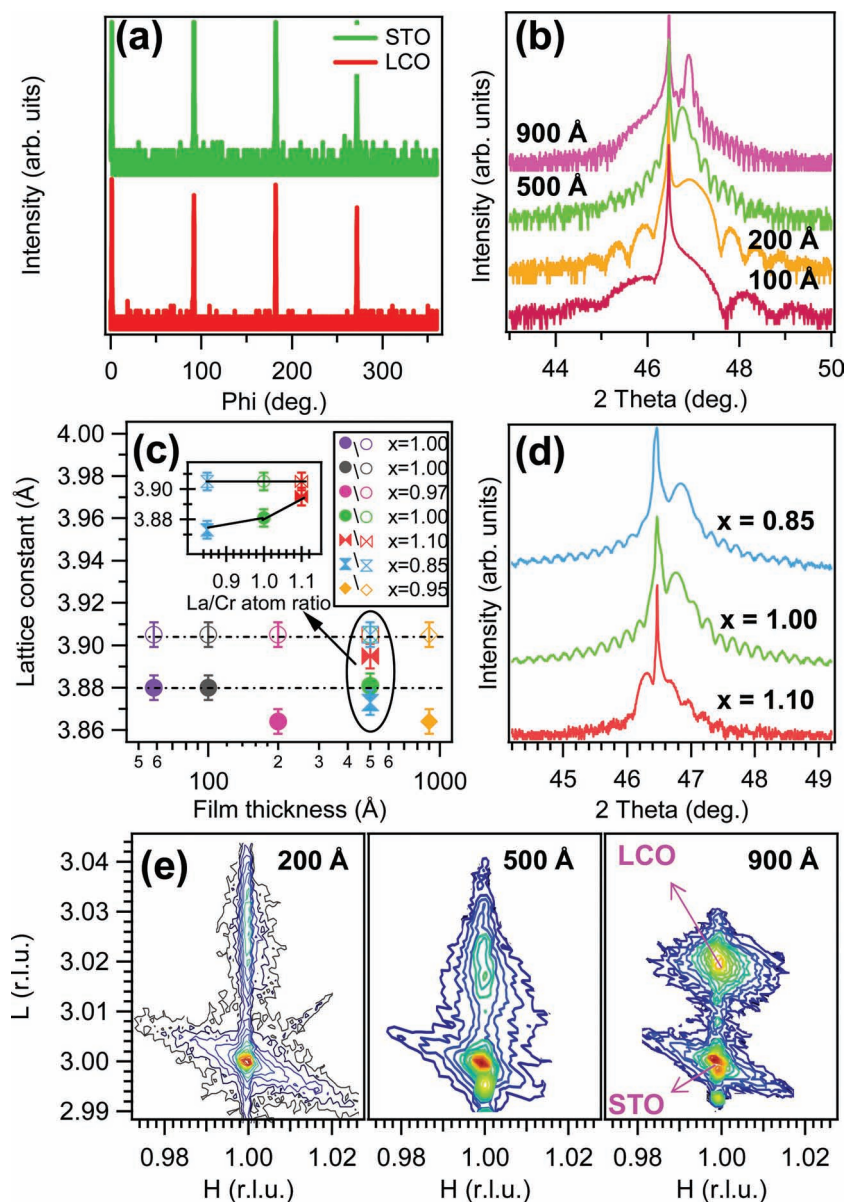the interface needs to be considered for the interstitial La defect.

The phase diagram for all considered defects is shown in **Figure 4**. The dashed horizontal line indicates the oxygen chemical potential calculated taking into account the background O_2 pressure and substrate temperature during the LCO film deposition.[37] These calculations reveal that structurally perfect LCO as well as LCO with La and Cr vacancies, and with both kinds of anti-site defects, are energetically feasible; their relative contributions can be controlled by the varying the La:Cr ratio. Interstitial Cr and La defects can be disregarded because their formation requires much lower oxygen pressures than what was used in this work.

The effect of these defects on the lattice parameter c is also shown in Figure 4. The optimal c for the defect-free epitaxial LCO is 3.820 Å. For the considered concentration of the La and Cr vacancies ($\approx$3%), the value of c decreases by 19 and 8 mÅ, respectively. The value of c increases by 34 mÅ in the case of La_{Cr} and decreases by 6 mÅ in the case of Cr_{La}. Since the La and Cr vacancies are stable in a relatively narrow range of the La:Cr ratio only, we conclude that the observed expansion of both c and the unit cell volume with increasing x (Figure 3c) can be ascribed to anti-site defects. The dependence of c on x can be qualitatively accounted for if we consider the ionic radii of La^{3+} (1.03 Å) and Cr^{3+} (0.62 Å).[38] However, the non-symmetric change of c (+0.034 Å for La_{Cr} and –0.006 Å for Cr_{La}) suggests that the size effect is only one factor contributing to this dependence, and that the co-existence of several types of defects may be important. For example, if La_{Cr} defects and Cr vacancies are present in comparable concentrations in La-rich LCO, their average effect on the value of c would be +34–19 = 15 mÅ, which is close to what is observed experimentally. In addition, cation defects modify the magnetic structure of LCO. Indeed, La_{Cr} can be considered as a vacant spin site in the G-type antiferromagnetic network of LCO, while in the case of Cr_{La}, substitutional Cr couples ferromagnetically with half of the nearest lattice Cr ions and antiferromagnetically with the other half. Such perturbations of the magnetic order result in larger interatomic distances locally and contribute to the increase of c. These magnetic defects, together with the ion size effect, introduce disorder into the film, thus decreasing film quality, as observed.

Coherent in-plane strain is also revealed by the (103) reciprocal space maps (RSMs) for a series of stoichiometric films in Figure 3e. There is no change in the out-of-plane momentum transfer between substrate and film for any of these samples. From the RSMs, it is also clear that film and substrate peaks have the same FWHM along H, revealing comparable crystal quality. The larger film FWHM along L results from finite-size broadening. The critical thickness for near stoichiometric film exceeds 900 Å, which is at least five times larger than the theoretical predication (183 Å) based on an elastic theory model.[36]

Cross-sectional high- and low-angle annular dark field scanning transmission electron microscopy (HAADF/LAADF-STEM) imaging provides corroborative insight into the structural quality

Materials Views
www.MaterialsViews.com

ADVANCED
FUNCTIONAL
MATERIALS
www.afm-journal.de

FULL PAPER

Figure 3. a) Representative in-plane x-ray diffraction {110} ϕ scans for a stoichiometric LCO film and its STO(001) substrate. b) High-resolution XRD patterns near the (002) Bragg peak for four near-stoichiometric LCO films with different thickness: 100 Å ($x = 1.00$), 200 Å ($x = 0.97$), 500 Å ($x = 1.00$) and 900 Å ($x = 0.94$). c) Lattice parameters (both in-plane, open circles, and out-of-plane, closed circles) for a series of films as a function of film thickness. The dashed lines denote the lattice parameters for coherently strained thin ($\leq$100 Å) films of stoichiometric LCO. The inset shows the lattice parameters as a function of film stoichiometry for three 500 Å LCO films with different x values. d) High-resolution XRD patterns near (002) Bragg peak for three 500 Å LCO films with different x values. e) (103) Reciprocal space maps for stoichiometric LCO films with different thicknesses. Both axes are referenced to the reciprocal lattice dimensions of STO (1 r.l.u. = $2\pi/3.905$ Å).

and defect formation in both stoichiometric and nonstoichiometric films. HAADF-STEM is primarily sensitive to atomic number, but also somewhat sensitive to crystal quality (channeling), while LAADF-STEM is more sensitive to diffraction contrast and strain. For the case of nominally stoichiometric 500 Å LCO, HAADF-STEM intensity is fairly uniform for the first ≈20 nm of the LCO, but decreasingly so near the surface, as shown in **Figure 5**a,c. The

intensity is also lower near the surface, suggestive of either poorer crystal quality or a lower average Z (by volume), or both (these two effects are frequently coupled.) As there was no demonstrable difference in the La:Cr ratio by EDS, and in light of the Rutherford backscattering spectrometry (RBS) results, the former explanation seems more likely. LAADF-STEM images in Figure 5b,d support this argument, with strong and clear strain contrast visible again after the first ≈20 nm of the film. This observation is also consistent with the higher background intensity in rocking curve scan for this film (see Supporting Information, inset of Figure 2d). Despite the apparent lines of strain contrast, there is no evidence for out-of-plane dislocations in STEM, more traditional dark-field transmission electron microscopy or high-resolutiuon transmission electron microscopy. The additional LAADF-STEM contrast at the LCO/STO interface is typical of heteroepitaxially grown films. HAADF-STEM imaging also supports a diffuse interface.

In contrast, the 500 Å film for which $x = 1.10$ has a highly defective interface with frequent encapsulated pockets of amorphous material (**Figure 6**). There is a more severe lateral inhomogeneity visible by HAADF-STEM (compare Figure 6a and Figure 5a). The encapsulated amorphous regions range in size from only a few unit cells (hardly differentiable from a dislocation core in cross-section) to tens of nanometers (Figure 6b). The regions of the film above these defects are typically marked by defects and stacking faults. This result is consistent with AFM and RHEED observations. For the smaller inclusions, this typically resulted in a fairly coherent fault extending from the interface to the surface. Above the larger, roughly pyramid-shaped amorphous inclusions, the lattice planes bow upward, resulting in a lower-angle grain boundary. To more clearly demonstrate this result, a simple trick of laterally (along the [100] direction) compressing magnified images is employed for typical smaller (Figure 6c,e) and larger (Figure 6d,f) amorphous inclusions. X-ray energy dispersive spectra confirmed that the amorphous regions predominantly contain La and Cr, albeit with varying La:Cr ratios and, in some cases, a significant fraction of Sr.

2.3. Local Structure

Crystallographic quality and the local structural environments about La and Cr sites were also determined by RBS in channeling mode and rocking-curve measurements. **Figure 7**a shows the RBS spectra in both channeling and random directions for

ADVANCED
FUNCTIONAL
MATERIALS
www.afm-journal.de

Materials
Views
www.MaterialsViews.com
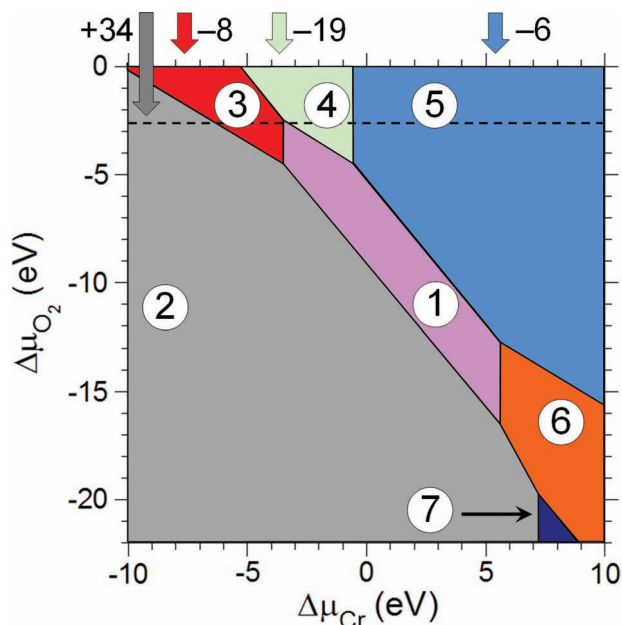
Figure 4. Phase diagram of the preferential cation defects in epitaxially strained LCO: 1: non-defective LCO supported on STO(001); 2: anti-site defect La_{Cr}; 3: neutral Cr vacancy; 4: neutral La vacancy; 5: anti-site defect Cr_{La}; 6: interstitial Cr; and 7: interstitial La. The numbers at the top of the figure show the changes of the c lattice parameter (in mÅ) for the considered La:Cr ratios. The horizontal dashed line indicates the oxygen chemical potential corresponding to the O_2 background pressure and the substrate temperature during the LCO film deposition.

films with different La-to-Cr atom ratios. The channeling spectra for both stoichiometric and Cr-rich films show low yield in the La surface peak region and a small extent of dechanneling. In contrast, the channeling spectrum for the La-rich film exhibits high counts in the La peak and more extensive dechanneling. A

small energy window to the left of the La surface peak was used to determine the minimum yield (χ_{min}), which is the ratio of the yield in the channeling geometry to that in a random direction. The χ_{min} values are 1.21%, and 0.64% for the stoichiometric and Cr-rich films, respectively, revealing excellent crystalline quality. In contrast, χ_{min} is 8.36% for the La-rich film, revealing substantial disorder, consistent with the XRD results.

Additional insight into the structural quality of these specimens can be gained from RBS rocking curve measurements. We show in Figure 7b an RBS spectrum indicating the La regions of interest (LCO film surface, LCO/STO interface, and La diffusion into the STO substrate) and in Figure 7c–e we plot the La angular scans along [001] for three different La-to-Cr atom ratios. The yields are integrated over the same depth regions for each of the films, and have been normalized by the values obtained in the random direction. Figure 7c shows RBS angular scans of the three La-containing regions for the stoichiometric sample, along with Sr signal from STO(001). The intensity minimum for the near-interface La is as low as that for Sr, revealing that La is as well ordered in the A sites as is Sr. In contrast, the La "surface" yield along the channeling direction doesn't drop as much as that for both Sr and near-interface La, indicating disorder in the near-surface region, possibly due to surface oxidation to $LaCrO_4$ due to air exposure.[35,36] There is no evidence for interstitial La near the interface. Interstitial La would result in a small peak at the bottom of the rocking curve for indiffused La. Additionally, indiffused La exhibits a rocking curve similar to that of Sr, indicating that indiffused La atoms are predominantly at Sr sites in the STO.

The critical angle (ψ_c) for channeling is also an important factor in RBS rocking-curve measurements since it is directly related to atomic displacements. Based on Lindhard's continuum mode,[39–43] the measured half-width ($\psi_{1/2}$) of an angular scan depends on two characteristic distances, the minimum distance for channeling (r_{min}) and the Thomas-Fermi screening length (a). The relevant formula is,

$$\psi_{\frac{1}{2}} = \psi_c = \psi_1 \left[\frac{1}{2} \ln \left(\frac{3a^2}{r_{min}^2} + 1 \right) \right]^{\frac{1}{2}} \quad (1)$$

where r_{min} is the estimated minimum distance an ion travels to remain in the channeling direction in the continuum model, and is a function of the thermal vibration amplitude (ρ) and the projected atomic displacement (u), as viewed along channeling direction. Both ψ_1 and a are functions of the target atomic number (Z_2) and the lattice spacing (d) along the channeling direction. The relevant formulas are $\psi_1 = (2Z_1 Z_2 e^2 / Ed)^{1/2}$ and $a = 0.8853 a_0 (Z_1^{1/2} + Z_2^{1/2})^{-2/3}$, where Z_1 is the projectile atomic number, E is the projectile energy, and a_0 is the Bohr radius. Thus, $\psi_{1/2}$ is directly dependent on the values of three factors: the target atomic number (Z_2), the atom displacement (u) and the lattice spacing (d). Thus, the observation of a larger
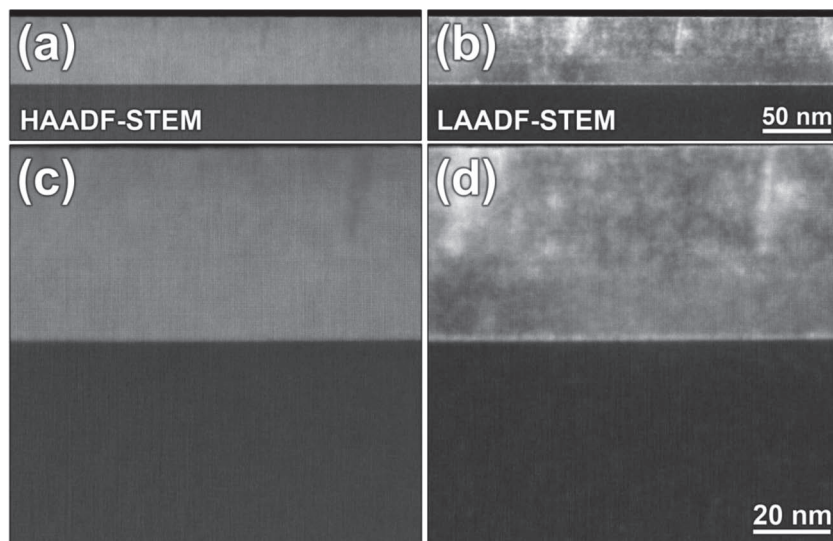
Figure 5. a,b) Lower and c,d) higher-magnification STEM images from a single representative region of a stoichiometric 500 Å-thick epitaxial LCO film on STO(001), taken in both HAADF-STEM (a,c) and LAADF-STEM (b,d) modes. Both demonstrate a fairly uniform film in the initial ≈20 nm and minor inhomogeneities in the final ≈30 nm.
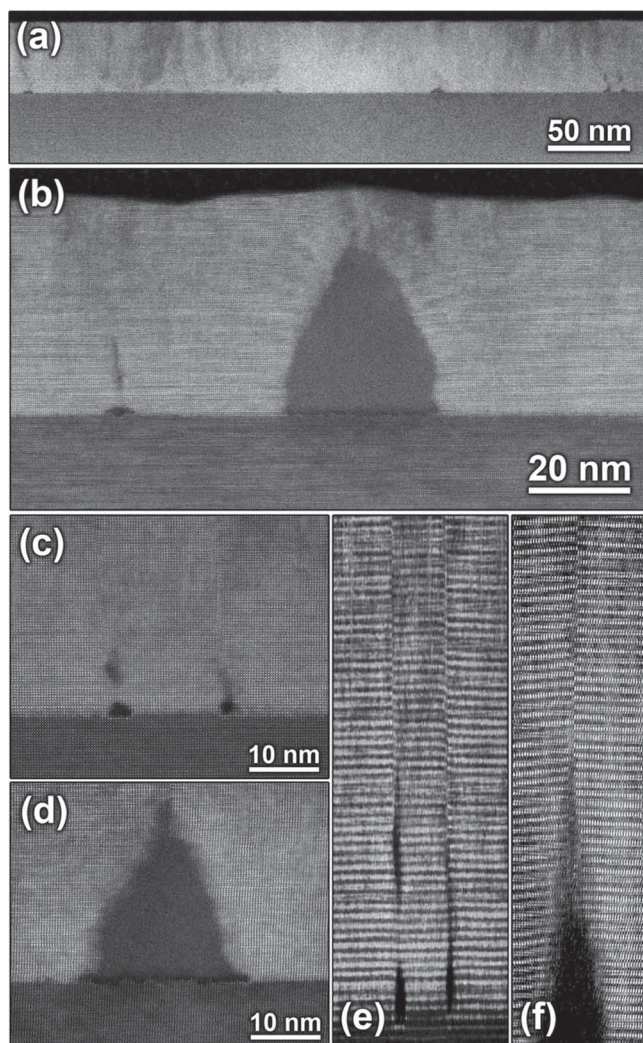
Figure 6. HAADF-STEM images of the characteristic defects in the La-rich ≈500 Å-thick LCO film. a) At lower magnifications one can see the high density of defects just above the LCO/STO interface, as well as the general in-plane inhomogeneity within the LCO film. b) These defects vary in size from sub-nanometer to tens of nanometers, and would substantially account for the surface roughness and poorer crystal quality observed by other the techniques employed in this work. The regions above these inclusions can be viewed as grain boundaries, punctuated with defects. To illustrate the shift in the (001) planes near these defects, magnified images of the regions immediately above typical defects (c,d) have been severely compressed along a [100] direction (e,f). For typical smaller inclusions (c,e) the boundaries are fairly coherent stacking faults along [001]. For larger inclusions (d,f) the planes are further bowed, resulting in junctions more like typical low-angle grain boundaries.

$\psi_{1/2}$ for La (both near-surface and near-interface) than for Sr is ascribed to the larger Z for La and the smaller lattice spacing along [001] direction for the LCO film than for bulk STO. However, the value of $\psi_{1/2}$ for indiffused La is lower than that for La in the bulk of the film, or for Sr in the STO. This result suggests that interdiffused La atoms are slightly laterally displaced as viewed along [001]. Calculations also indicate that while the displacements for Sr in the STO substrate and La away from

the interface are ≈0.01 and 0.02 Å, respectively, the estimated lateral displacement for indiffused La atoms within the STO is in excess of ≈0.04 Å. This result is not unexpected considering that the interface is a quaternary due to site exchange for all four cations.
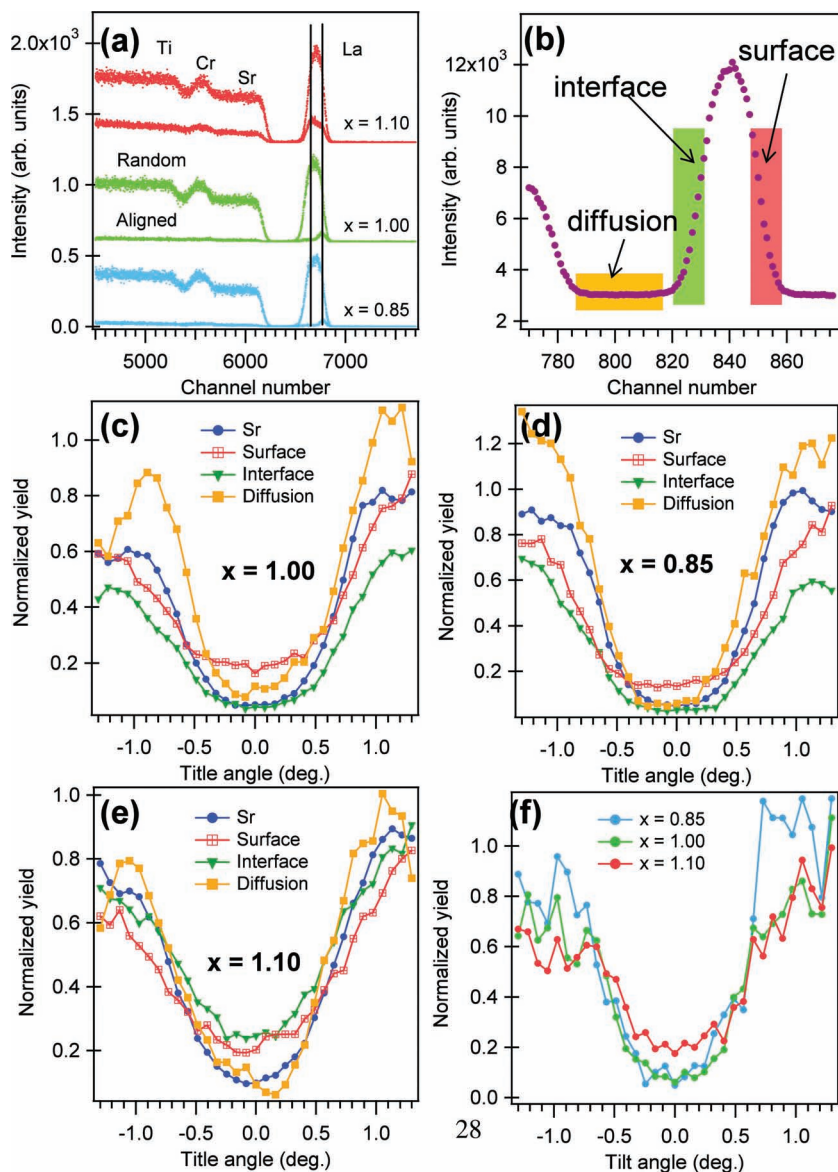
The rocking curves for the Cr-rich film are shown in Figure 7d and exhibit nearly the same behavior as those for the stoichiometric film, indicating a high degree of crystal quality near the interface, slight disorder near film surface, and substitutional La at Sr sites within the mixed region. However, the structural quality of the La-rich film is lower than that of other two as revealed by the higher values of the intensity minima at 0° tilt angle, as seen Figure 7e.

We have also measured rocking curves for Cr backscattering for these three films. Due to the much lower RBS sensitivity for Cr compared to La, the counting statistics are not as good as for La. Nevertheless, some qualitative similarities exist. As seen in Figure 7f, the angular scan for the La-rich film exhibits a higher intensity at the minimum value than the other two films, revealing more structural disorder throughout the La-rich film, consistent with RBS and XRD. Therefore, disorder occurs not only at the La site, but also at the Cr site in the La-rich film.

2.4. Interdiffusion at the Interface

Figure 8a shows random RBS spectra for the three LCO films with different La:Cr ratios measured at a scattering angle of 150°. This geometry yields better mass resolution due to the shorter path-length for the backscattered beam and minimal inelastic-scattering-induced broadening. By performing least-squares fits to RBS simulations, we are able to obtain quantitative atomic percentages for both cations.[36] The RBS La:Cr ratios for the three films were 0.85, 1.00 and 1.10, as used throughout the text up to this point for these samples. We fit the spectra (using SIMNRA) with both abrupt and optimized intermixing models, as displayed in Figure 8a,b. The abrupt model does not predict the nonzero counts in the valley between low-energy side of La peak and leading edge of Sr plateau. In order to predict the presence of counts in the valley, indiffusion of La and outdiffusion of Sr must be included in the model. The statistical noise associated with the low counts in the valley precludes obtaining a clear best fit to any one diffusion profile. However, the La atom profile which qualitatively accounts for the x = 1.00 spectrum is shown in Figure 8c. This diffusion profile is modeled as discrete compositional steps in which the La concentration beings to drop before arriving at the interface (at a depth of ≈500 Å) and persists to a depth of more than 1000 Å, albeit at very low concentrations. Together with the rocking curve data shown in Figure 7, these spectra show that A-site intermixing occurs to comparable extents in all three samples.

We now consider the roles of deposition temperature and substrate surface quality in promoting intermixing. To determine the effect of temperature, we grew a 500 Å stoichiometric, but amorphous LCO film on STO at ambient temperature. The amorphous character of the film was confirmed by RHEED and XRD. The RBS spectrum for this amorphous film is

**ADVANCED
FUNCTIONAL
MATERIALS**
www.afm-journal.de

**Materials
Views**
www.MaterialsViews.com

Figure 7. a) Random and channeling RBS spectra obtained using 2.0 MeV He$^+$ ions at a scattering angle of 150° for LCO films for different x. b) The three spectral windows at which we carried out La angular scans and the depths at which counts in these windows originate ("diffusion" refers to La which diffuses into the STO). c–e) RBS angular scans of the three La-containing film regions along with the Sr scan for STO(001) for stoichiometric ($x = 1.00$), Cr-rich ($x = 0.85$), and La-rich LCO ($x = 1.10$) films, respectively. f) Cr RBS angular scans for the three LCO films.

shown and compared to that for an analogous epitaxial film in **Figure 9**a. Interestingly, the amorphous film exhibits an extent of intermixing similar to that of the epitaxial film, based on the nonzero counts in the valley between the La and Sr peaks (Figure 9b). This result reveals that intermixing is not driven purely by kinetic forces and cannot be quenched simply by reducing the substrate temperature.

We thus focus on the role of substrate quality. The TiO$_2$-terminated STO(001) substrates used here were prepared using the popular HF-etch and O$_2$ tube furnace anneal method. This process typically results in measurable F contamination on

the free STO(001) surface.[44] The presence of F on the STO surface is not likely in and of itself to promote cation mixing. However, sub-surface cation vacancies resulting from the associated high-temperature O$_2$ tube-furnace anneal could do so. In order to disentangle these two possible effects, we replaced the HF etch with a deionized (DI) water etch surrounded by a pair of tube furnace anneals, as described in the Supporting Information, and then deposited epitaxial LCO. RBS shows that LCO films deposited on both HF- and DI-water etched substrates exhibit similar extents of interfacial mixing (see Supporting Information Figure 4), revealing that it is not the HF etch per se that causes cation mixing. Rather, XPS suggests that high-temperature annealing creates Sr vacancies which promote La indiffusion, as discussed in the Supporting Information. It has been shown elsewhere that annealing the TiO$_2$-terminated STO at 600 °C in oxygen ambient results in Sr vacancies creation at substrate surface.[12,45,46] Therefore, we hypothesize that Sr vacancy defects, resulting from tube furnace anneal required generating a TiO$_2$-terminated surface, promotes La indiffusion. As a test of this hypothesis, we grew an amorphous, stoichiometric LCO film on Si(001) at ambient temperature with the same atom fluxes those used to grow on STO at room temperature. The RBS spectrum for this film is shown in Figure 9a,b. In contrast to the LCO/STO interface prepared at room temperature, the LCO/Si interface is rather abrupt, as revealed by the absence of counts in the valley between the Cr and La peaks. This result supports our hypothesis, as electronic grade crystalline Si(001) is largely defect free.

Finally, we explore the role of deposition technique in driving interfacial mixing. We compare LCO deposited at ambient temperature on Si(001) by MBE (Figure 9c,d) with LaAlO$_3$ (LAO) deposited at ambient temperature on Si(001) by off-axis PLD at 10 mTorr O$_2$ (Figure 9e,f). We did not deposit LCO by PLD because we were unsuccessful at fabricating a robust ablation target for LCO. In stark contrast to the rather abrupt LCO/Si interface prepared by MBE, the LAO/Si interface exhibits considerable La indiffusion, as revealed by the presence of counts in the valley between the La and Al peaks in Figure 9f. This result is strongly suggestive of La implantation into Si as a result of energetic ions in the ablation plume, even at the relatively high O$_2$ pressure of 10 mTorr. The laser energy density on the single-crystal LAO target in the PLD system was ≈3 J cm^{-2}, and this power level appears to give rise to ions in the plume that are sufficiently energetic to implant into crystalline Si.
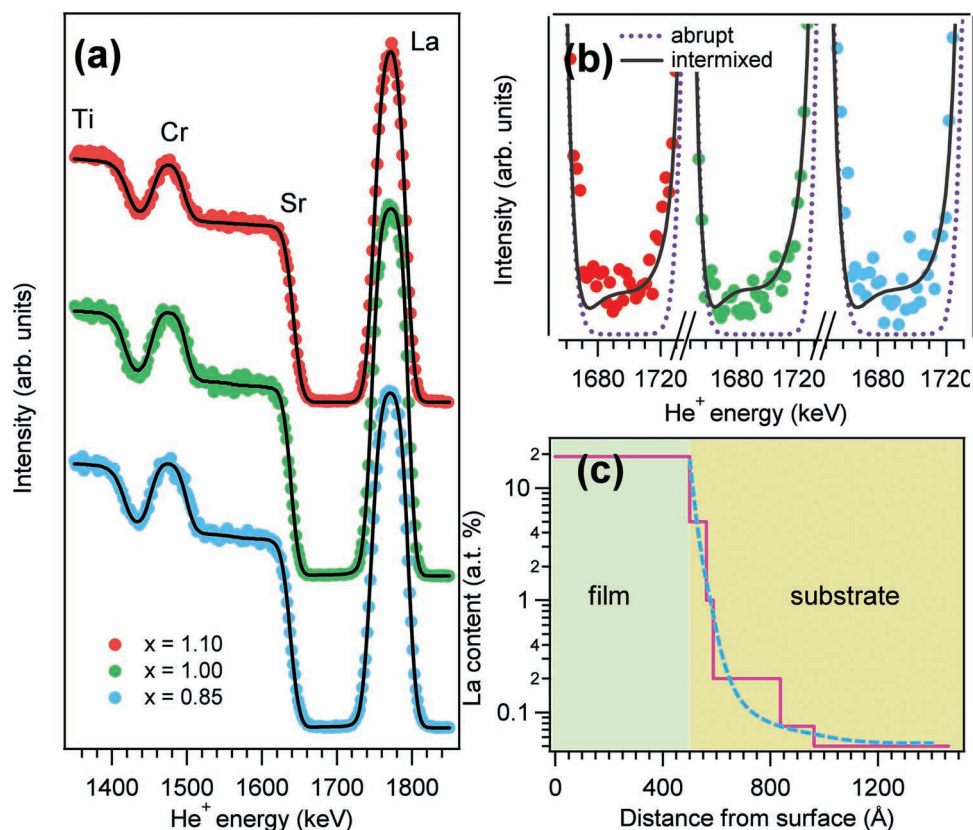
Figure 8. a) RBS spectra in the random geometry (solid circles) and SIMNRA simulations (solid curves) for LCO films with different *x* values. b) Close-up view of La-Sr valley for each film, along with simulations using both abrupt (dots) and intermixed (solid curves) interface models. c) The La atom profile used in the intermixed interface simulation for the 500 Å stoichiometric LCO film.
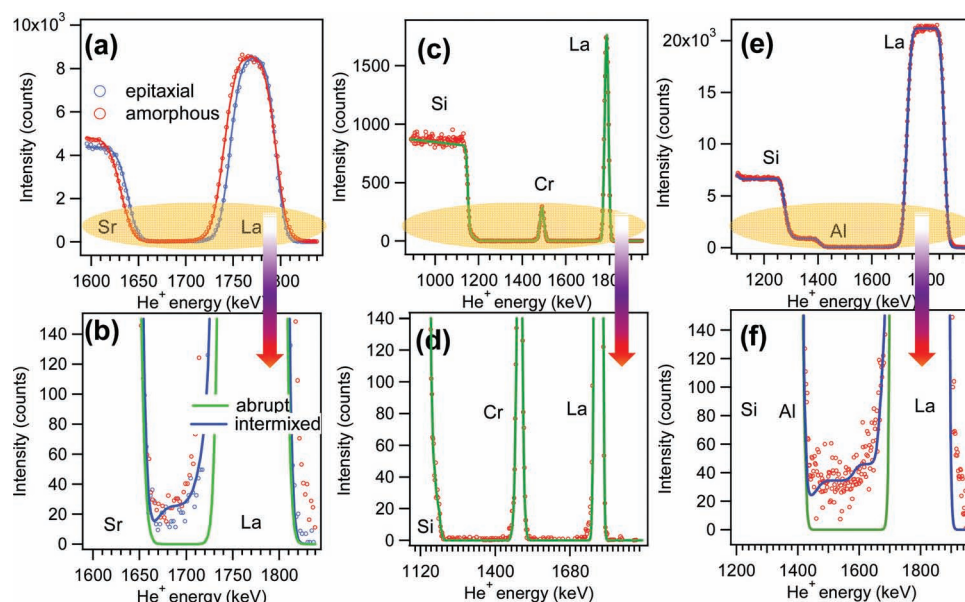
Figure 9. a) RBS spectra in the random geometry (solid circles) for 500 Å-thick, MBE-grown epitaxial and amorphous LCO films on STO(001), along with simulations using both abrupt (green curve) and intermixing (blue curve) models of the interface. b) Close-up view of the La-Sr valley for each film, along with the same simulations. c,d) RBS for a 180 Å-thick, MBE-grown LCO film grown on Si(001) at ambient temperature along with an abrupt-interface simulation. e,f) RBS for a 580 Å-thick, PLD-grown LAO film grown on Si(001) at ambient temperature, along with both abrupt (green curve) and intermixing (blue curve) interface simulations.

**ADVANCED
FUNCTIONAL
MATERIALS**
www.afm-journal.de

*Materials
Views*
www.MaterialsViews.com

FULL PAPER

3. Conclusion

We have brought several complementary analytical techniques, along with ab initio simulations, together to investigate the effect of cation stoichiometry and substrate surface quality on the crystallinity, surface morphology, interfacial mixing, and defect generation in MBE-grown films of the polar perovskite oxide LaCrO₃ on SrTiO₃(001). We find that this material is able to accommodate La-to-Cr ratios which differ from unity by as much as ≈15% in the Cr rich direction without extensive loss of structural quality. The material buckles structurally more readily in the La-rich direction. In both directions, our data and calculations are consistent with cation anti-site defect formation as a way the LCO lattice can accommodate La-to-Cr atom ratio mismatches. If we go far enough in the La-rich direction (i.e., to La:Cr = 1.25), excess La is expelled by the lattice into a disordered secondary phase (La_2O_3). Cation mixing occurs at the interface for all film compositions, and is not affected by stoichiometry in any obvious way. Comparison of data for LCO/STO(001) with that for LCO/Si(001), both prepared at ambient temperature, reveals that interfacial mixing is driven at least in part by defects in the STO. Likewise, comparison of MBE-grown LCO/Si(001) with PLD-grown LaAlO₃ (LAO)/Si(001), both prepared at ambient temperature, shows that the higher energies of atoms and ions in the laser ablation plume drive interfacial mixing more than occurs in MBE, with its lower atom energies. These results provide guidelines and a framework for understanding the best ways to prepare complex oxide heterojunctions for either fundamental materials research or novel device fabrication. In particular, this study demonstrates that the compositions of both BO_2 and AO sublattices of LCO can deviate significantly from the ideal stoichiometry without inducing major lattice structure changes. Given that electronic, magnetic and optical properties can be substantially changed by much smaller changes in composition, we conclude that structural analysis alone provides inadequate characterization of these materials and can, in turn, lead to misleading interpretation of the observed physical phenomena.

4. Experimental and Theoretical Section

As-received STO substrates were etched in buffered HF and annealed in air to produce TiO₂-terminated STO as described elsewhere.[47] Following sonication in acetone, isopropanol and distilled water, the substrates were loaded into a custom MBE chamber and exposed to activated oxygen from an electron cyclotron resonance plasma at a chamber pressure of 2.0×10^{-5} Torr for 30 min, resulting in no detectable carbon by XPS.[48,49] During LCO deposition, the oxidant was O₂ at a pressure of ≈6.0×10^{-8} Torr, as determined by a residual gas analyzer, and the substrate temperature was 650 ± 50 °C, as measured by a two-color infrared pyrometer. Cr was deposited using an electron beam evaporator and the sublimation rate was monitored and controlled using in situ atomic absorption (AA) spectroscopy. La was evaporated using a high-temperature effusion cell and the La rate was measured before and after deposition with a QCO positioned at the substrate position. The Cr flux was adjusted through (AA) feedback control to achieve different La-to-Cr ratios (x). The typical growth rate was ≈40 s per unit cell (u.c.). The O₂ valve was closed immediately after growth and samples were cooled to room temperature in high vacuum to prevent oxidation of structural Cr³⁺ in the near-surface region of LCO to Cr⁵⁺ or Cr⁶⁺.[35,36]

Film growth and surface quality were monitored by in situ RHEED at 15 keV. Generally, film growth was terminated when the RHEED specular beam intensity was at a maximum, if intensity oscillations were observed, to insure the deposition of an integer number of unit cells. Film thickness was determined by counting RHEED oscillations (if present), as well as from X-ray reflectivity and RBS. Film thicknesses ranged from 100 to 900 Å. Film composition was determined by in situ high-energy-resolution XPS using a Scienta SES 200 electron energy analyzer with a monochromatic Al $K\alpha$ X-ray source. La-to-Cr atom ratios were determined from La 4d and Cr 3p peak area ratios by calibrating with RBS and using SIMNRA simulations[50] on select samples. Local structure at specific sites was determined using RBS rocking curve measurements. Surface morphology was measured ex situ by tapping-mode AFM using a Digital Instruments Nanoscope III. Lattice parameters and overall crystal quality were determined using high-resolution XRD and reciprocal space mapping with a Philips X'Pert diffractometer equipped with a Cu anode. A hybrid monochromator, consisting of four-bounce double crystal Ge (220) and a Cu X-ray mirror, was placed in the incident beam path to generate monochromatic Cu $K\alpha$ X-rays (λ = 1.54056 Å) with a beam divergence of 12 arc seconds. Crystal quality was determined by means of triple-axis rocking curve measurements in which an additional three-bounce Ge (220) channel-cut analyzer was placed in front of a proportional counter to obtain the same divergence as the incident beam. Select films were examined in cross-section using conventional TEM and STEM with a probe-corrected FEI Titan microscope operated at 300 kV. X-ray energy dispersive spectra were also collected in STEM at 300 kV with a 0.13 mrad EDAX detector. Cross-sections were prepared with an FEI Helios dual-beam FIB/SEM equipped with an Omniprobe manipulator using the lift-out technique and further thinned on a liquid nitrogen cooled stage with an Ar-ion source (0.5–2 kV), using a Fischione NanoMill.

The relative stability of cation anti-site defects and neutral La and Cr vacancies and interstitials were calculated using a method developed for comparison of the free energies of surfaces with different stoichiometries.[37,51,52] In our case, this method allows one to determine preferential defect structures in the Cr-rich (La-poor) and Cr-poor (La-rich) conditions as a function of oxygen pressure and temperature. The free energies for solids have been approximated using the corresponding total energies calculated using the density functional theory; the density functional optimized for solids by Perdew et al. (PBEsol)[53] and the projected augmented waves method,[54] as implemented in the Vienna ab initio simulation program (VASP) code[55] were used. The plane-wave basis set cutoff was set to 500 eV. All calculations were performed using the 2 $\sqrt{2}a_0 \times 2 \sqrt{2}a_0 \times 4c$ supercell and the Γ point of the Brillouin zone. The in-plane lattice constant was fixed at the value corresponding to that of the bulk SrTiO₃ (a_0 = 3.905 Å). The total energy was minimized with respect to the value of the lattice constant c and internal coordinates of all atoms until the forces acting on atoms are below 0.01 eV Å⁻¹.

Supporting Information

Supporting Information is available from the Wiley Online Library or from the author.

Acknowledgements

[1] A. Ohtomo, H. Y. Hwang, *Nature* **2004**, *427*, 423.

[2] S. Thiel, G. Hammerl, A. Schmehl, C. W. Schneider, J. Mannhart, *Science* **2006**, *313*, 1942.

[3] M. Huijben, G. Rijnders, D. H. A. Blank, S. Bals, S. Van Aert, J. Verbeeck, G. Van Tendeloo, A. Brinkman, H. Hilgenkamp, *Nat. Mater.* **2006**, *5*, 556.

[4] N. Reyren, S. Thiel, A. D. Caviglia, L. F. Kourkoutis, G. Hammerl, C. Richter, C. W. Schneider, T. Kopp, A.-S. Ruetschi, D. Jaccard, M. Gabay, D. A. Muller, J.-M. Triscone, J. Mannhart, *Science* **2007**, *317*, 1196.

[5] N. Nakagawa, H. Y. Hwang, D. A. Muller, *Nat. Mater.* **2006**, *5*, 204.

[6] M. Salluzzo, J. C. Cezar, N. B. Brookes, V. Bisogni, G. M. Luca, C. Richter, S. Thiel, J. Mannhart, M. Huijben, A. Brinkman, G. Rijnders, G. Ghiringhelli, *Phys. Rev. Lett.* **2009**, *102*, 166804.

[7] A. Savoia, D. Paparo, P. Perna, Z. Ristic, M. Salluzzo, F. Miletto Granozio, U. Scotti di Uccio, C. Richter, S. Thiel, J. Mannhart, L. Marrucci, *Phys. Rev. B* **2009**, *80*, 075110.

[8] A. Kalabukhov, R. Gunnarsson, J. Borjesson, E. Olsson, T. Claeson, D. Winkler, *Phys. Rev. B* **2007**, *75*, 121404(R).

[9] G. Herranz, M. Basletic, M. Bibes, C. Carretero, E. Tafra, E. Jacquet, K. Bouzehouane, C. Deranlot, A. Hamzic, J.-M. Broto, A. Barthelemy, A. Fert, *Phys. Rev. Lett.* **2007**, *98*, 216803.

[10] W. Siemons, G. Koster, H. Yamamoto, W. A. Harrison, G. Lucovsky, T. H. Geballe, D. H. A. Blank, M. R. Beasley, *Phys. Rev. Lett.* **2007**, *98*, 196802.

[11] P. R. Willmott, S. A. Pauli, R. Herger, C. M. Schleputz, D. Martoccia, B. D. Patterson, B. Delley, R. Clarke, D. Kumah, C. Cionca, Y. Yacoby, *Phys. Rev. Lett.* **2007**, *99*, 155502.

[12] A. S. Kalabukhov, Y. A. Boikov, I. T. Serenkov, V. I. Sakharov, V. N. Popok, R. Gunnarsson, J. Borjesson, N. Ljustina, E. Olsson, D. Winkler, T. Claeson, *Phys. Rev. Lett.* **2009**, *103*, 146101.

[13] S. A. Chambers, M. H. Engelhard, V. Shutthanandan, Z. Zhu, T. C. Droubay, L. Qiao, P. V. Sushko, T. Feng, H. D. Lee, T. Gustafsson, E. Garfunkel, A. B. Shah, J. M. Zuo, Q. M. Ramasse, *Surf. Sci. Rep.* **2010**, *65*, 317.

[14] L. Qiao, T. C. Droubay, T. C. Kaspar, P. V. Sushko, S. A. Chambers, *Surf. Sci.* **2011**, *605*, 1381.

[15] D. H. Lowndes, D. B. Geohegan, A. A. Puretzky, D. P. Norton, C. M. Rouleau, *Science* **1996**, *273*, 898.

[16] D. Dijkkamp, T. Venkatesan, X. D. Wu, S. A. Shaheen, N. Jisrawi, Y. H. Minlee, W. L. McLean, M. Croft, *Appl. Phys. Lett.* **1987**, *51*, 619.

[17] B. Dam, J. H. Rector, J. Johansson, S. Kars, R. Griessen, *Appl. Surf. Sci.* **1996**, *96-8*, 679.

[18] T. Ohnishi, M. Lippmaa, T. Yamamoto, S. Meguro, H. Koinuma, *Appl. Phys. Lett.* **2005**, *87*, 241919.

[19] E. Breckenfeld, R. Wilson, J. Karthik, A. R. Damodaran, D. G. Cahill, L. W. Martin, *Chem. Mater.* **2012**, *24*, 331.

[20] D. S. Kan, Y. Shimakawa, *Appl. Phys. Lett.* **2011**, *99*, 081907.

[21] L. Qiao, T. C. Droubay, V. Shutthanandan, Z. Zhu, P. V. Sushko, S. A. Chambers, *J. Phys.: Condens. Matter* **2010**, *22*, 312201.

[22] T. C. Droubay, L. Qiao, T. C. Kaspar, M. H. Engelhard, V. Shutthanandan, S. A. Chambers, *Appl. Phys. Lett.* **2010**, *97*, 124105.

[23] T. Ohnishi, K. Takada, *Appl. Phys. Express* **2011**, *4*, 025501.

[24] Z. Marton, S. S. A. Seo, T. Egami, H. N. Lee, *J. Cryst. Growth* **2010**, *312*, 2923.

[25] S. Kobayashi, Y. Tokuda, T. Ohnishi, T. Mizoguchi, N. Shibata, Y. Sato, Y. Ikuhara, T. Yamamoto, *J. Mater. Sci.* **2011**, *46*, 4354.

[26] H. W. Jang, A. Kumar, S. Denev, M. D. Biegalski, P. Maksymovych, C. W. Bark, C. T. Nelson, C. M. Folkman, S. H. Baek, N. Balke, C. M. Brooks, D. A. Tenne, D. G. Schlom, L. Q. Chen, X. Q. Pan, S. V. Kalinin, V. Gopalan, C. B. Eom, *Phys. Rev. Lett.* **2010**, *104*, 197601.

[27] T. Ohnishi, K. Shibuya, T. Yamamoto, M. Lippmaa, *J. Appl. Phys.* **2008**, *103*, 103703.

[28] P. R. Willmott, J. R. Huber, *Rev. Mod. Phys.* **2000**, *72*, 315.

[29] H. M. Christen, G. Eres, *J. Phys.: Condens. Matter* **2008**, *20*, 16.

[30] S. A. Chambers, *Adv. Mater.* **2010**, *22*, 219.

[31] M. E. Klausmeierbrown, J. N. Eckstein, I. Bozovic, G. F. Virshup, *Appl. Phys. Lett.* **1992**, *60*, 657.

[32] Z. M. Wang, J. G. Feng, Y. Yang, Y. Yao, L. Gu, F. Yang, Q. L. Guo, J. D. Guo, *Appl. Phys. Lett.* **2012**, *100*, 051602.

[33] J. H. Haeni, C. D. Theis, D. G. Schlom, *J. Electroceram.* **2000**, *4*, 385.

[34] M. P. Warusawithana, C. Cen, C. R. Sleasman, J. C. Woicik, Y. L. Li, L. F. Kourkoutis, J. A. Klug, H. Li, P. Ryan, L. P. Wang, M. Bedzyk, D. A. Muller, L. Q. Chen, J. Levy, D. G. Schlom, *Science* **2009**, *324*, 367.

[35] S. A. Chambers, L. Qiao, T. C. Droubay, T. C. Kaspar, B. W. Arey, P. V. Sushko, *Phys. Rev. Lett.* **2011**, *107*, 206802.

[36] L. Qiao, T. C. Droubay, M. E. Bowden, V. Shutthanandan, T. C. Kaspar, S. A. Chambers, *Appl. Phys. Lett.* **2011**, *99*, 061904.

[37] K. Johnston, M. R. Castell, A. T. Paxton, M. W. Finnis, *Phys. Rev. B* **2004**, *70*, 085415.

[38] R. D. Shannon, C. T. Prewitt, *Acta Crystallogr. B* **1969**, *B 25*, 925.

[39] J. R. Tesmer, M. Nastasi, J. C. Barbour, C. J. Maggiore, J. W. Mayer, *Handbook of Modern Ion Beam Materials Analysis*, Materials Research Society, Pittsburgh, PA **1995**.

[40] D. S. Gemmell, *Rev. Mod. Phys.* **1974**, *46*, 129.

[41] S. T. Picraux, J. A. Davies, L. Eriksson, N. G. E. Johansso, J. W. Mayer, *Phys. Rev.* **1969**, *180*, 873.

[42] T. E. Derry, R. W. Fearick, J. P. F. Sellschop, *Phys. Rev. B* **1982**, *26*, 17.

[43] G. Bai, M. A. Nicolet, J. E. Mahan, K. M. Geib, *Phys. Rev. B* **1990**, *41*, 8603.

[44] S. A. Chambers, T. C. Droubay, C. Capan, G. Y. Sun, *Surf. Sci.* **2012**, *606*, 554.

[45] R. Meyer, R. Waser, J. Helmbold, G. Borchardt, *Phys. Rev. Lett.* **2003**, *90*, 105901.

[46] B. Jalan, S. Stemmer, S. Mack, S. J. Allen, *Phys. Rev. B* **2010**, *82*, 081103.

[47] L. Qiao, T. C. Droubay, T. Varga, M. E. Bowden, V. Shutthanandan, Z. Zhu, T. C. Kaspar, S. A. Chambers, *Phys. Rev. B* **2011**, *83*, 085408.

[48] T. C. Droubay, K. M. Rosso, S. M. Heald, D. E. McCready, C. M. Wang, S. A. Chambers, *Phys. Rev. B* **2007**, *75*, 104412.

[49] B. Zhao, T. C. Kaspar, T. C. Droubay, J. McCloy, M. E. Bowden, V. Shutthanandan, S. M. Heald, S. A. Chambers, *Phys. Rev. B* **2011**, *84*, 245325.

[50] M. Mayer, *SIMNRA User's Guide 6.04*, Max-Planck-Institut für Plasmaphysik, Garching, Germany **2008**.

[51] I. G. Batyrev, A. Alavi, M. W. Finnis, *Phys. Rev. B* **2000**, *62*, 4698.

[52] E. Heifets, S. Piskunov, E. A. Kotomin, Y. F. Zhukovskii, D. E. Ellis, *Phys. Rev. B* **2007**, *75*, 115417.

[53] J. P. Perdew, A. Ruzsinszky, G. I. Csonka, O. A. Vydrov, G. E. Scuseria, L. A. Constantin, X. L. Zhou, K. Burke, *Phys. Rev. Lett.* **2008**, *100*, 136406

[54] P. E. Blochl, *Phys. Rev. B* **1994**, *50*, 17953.

[55] G. Kresse, J. Furthmuller, *Phys. Rev. B* **1996**, *54*, 11169.